Remote Sensing of Environment 289 (2023) 113518

Contents lists available at ScienceDirect

Remote Sensing of Environment

journal homepage: www.elsevier.com/locate/rse

Modelling InSAR-derived hillslope velocities with multivariate statistics: A first attempt to generate interpretable predictions

Kun He [a,b], Hakan Tanyas [b,*], Ling Chang [b], Xiewen Hu [a], Gang Luo [a], Luigi Lombardo [b]

[a] Southwest Jiaotong University, Faculty of Geoscience and Environmental Engineering, Chengdu, China
[b] University of Twente, Faculty of Geo-Information Science and Earth Observation (ITC), Enschede, the Netherlands

ARTICLE INFO

Edited by Jing M. Chen

Keywords:
Hillslope deformation
InSAR
Prediction
Line-of-sight velocity
Multivariate regression
Sentinel-1
Spatio-temporal model

ABSTRACT

Spatiotemporal patterns of earth surface deformation are influenced by a combination of the geologic, topographic, seismic, anthropogenic, meteorological and climatic conditions specific to any landscape of interest. These have been mostly modelled through machine learning tools. However, these influences are yet to be explored and exploited to train interpretable data-driven models and then make predictions on the deformation one may expect in space or time. This work explored this aspect by proposing the first multivariate model dedicated to InSAR-derived deformation data. The results we obtain are promising for we suitably retrieved the signal of environmental predictors, from which we then estimated the mean line of sight velocities for a number of hillslopes affected by seismic shaking. The importance of such models resides in its potential for opening an entirely new research line for slope instability modelling.

1. Introduction

The last few decades have seen the birth of space-borne remote sensing and its consolidated use as a monitoring technique capable of sensing the earth's surface and the hazardous phenomena it hosts (Tralli et al., 2005). Among the available space-borne techniques, Interferometric Synthetic Aperture Radar (InSAR) gained the spotlight for its millimetre-level precision of the earth surface deformation (Hilley et al., 2004; Massonnet and Feigl, 1998). Following the launch of the Sentinel-1 mission, public radar scenes became publicly accessible over the whole planet with an orbital frequency of 6–12 days. This has further promoted the use of InSAR for monitoring surface deformations associated with land subsidence (Cigna and Tapete, 2021; Haghshenas Haghighi and Motagh, 2019), slow-moving hillslopes (Barra et al., 2016; Lacroix et al., 2020) and volcanic edifice (Gaddes et al., 2018; Xu et al., 2016). The most representative example of its use can be seen in the European project on surface deformation time series, spanning from 2015 to 2020, released by the European Ground Motion Service (Costantini et al., 2021; Crosetto et al., 2021).

To date though, the vast majority of InSAR applications have focused on observational research. In other words, despite the growing availability of surface motion data, limited efforts have been dedicated to linking its space-time patterns to environmental characteristics, thus moving away from descriptive analyses and toward predictive ones. Examples do exist where temporal statistics are used univariately to attempt a temporal prediction (Chen et al., 2021; Ding et al., 2021; He et al., 2022; Ma et al., 2020), although these techniques are purely based on the deformation signal itself, thus being poorly related to the environmental conditions responsible for the deformation in the first place (Intrieri et al., 2018; Palmer, 2017). The use of bivariate models has also been explored in the context of land subsidence, being correlated to groundwater depletion (Chaussard et al., 2013), or in the case of hillslope deformation, explained according to precipitation and/or seismicity (Bontemps et al., 2020). However, even these examples share a common limitation, this being the bivariate framework they have been based on so far. Such a structure may not be suited to welcome the complex interactions between various factors responsible for earth's surface changes; although they can still be useful to identify those factors that primarily drive the surface deformation (Dille et al., 2021). Ideally, a holistic modelling approach should be flexible enough to encompass various contributors to the earth's surface deformation. This is actually a common assumption in data-driven models built to estimate slope instabilities (Lombardo and Mai, 2018). Thus, it is reasonable to assume that the same is valid in the context of InSAR-derived hillslope deformation, yet these aspects are still mostly unexplored.

Two main obstacles may have been responsible for the limited

* Corresponding author.
E-mail address: h.tanyas@utwente.nl (H. Tanyas).

https://doi.org/10.1016/j.rse.2023.113518
Received 25 October 2022; Received in revised form 30 January 2023; Accepted 21 February 2023
Available online 27 February 2023

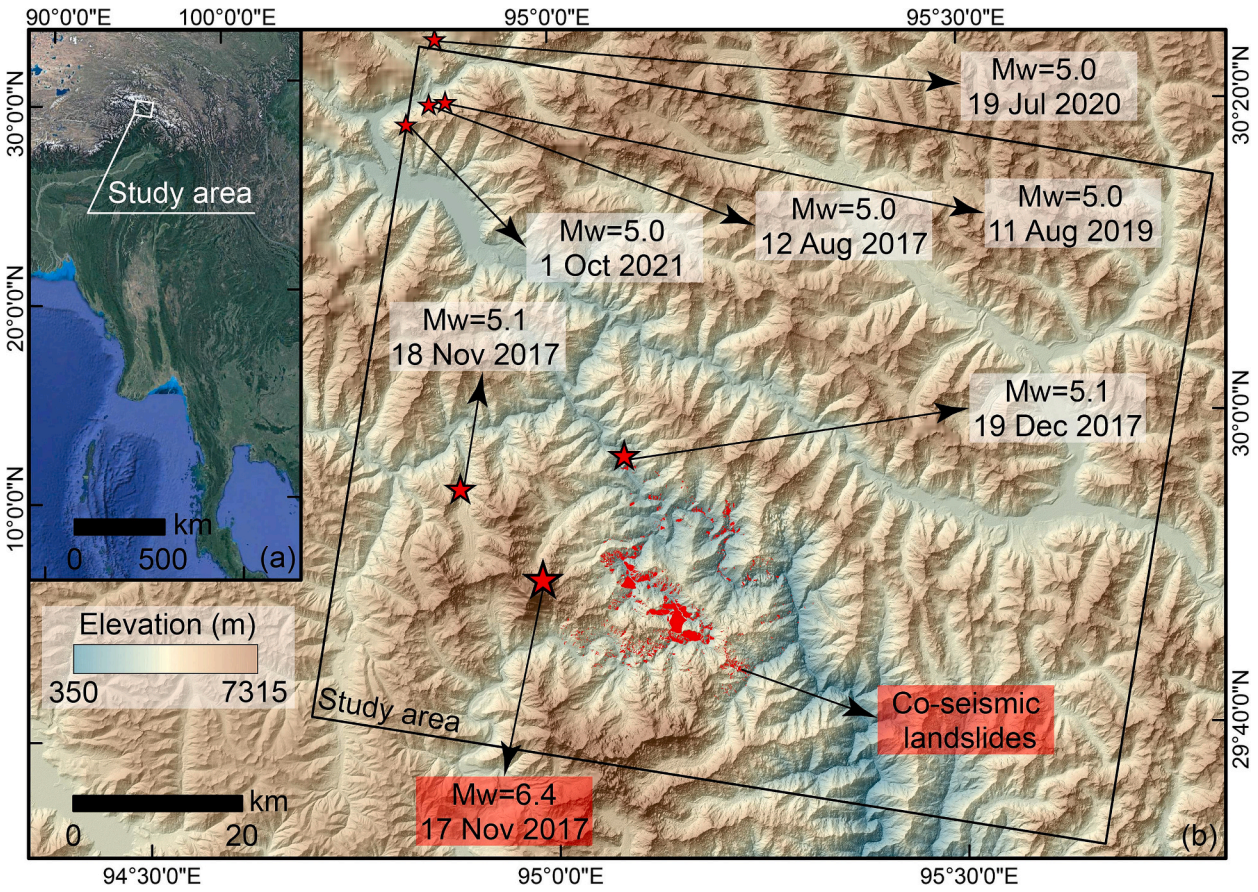

Fig. 1. Panels showing (a) the location of the study area over the Himalayan range and (b) a zoomed-in view of the study area overlaying by the epicentre of earthquakes (Mw $\geq$ 5.0) that occurred in the last five years and spatial distribution of co-seismic landslides triggered by the 2017 Mw 6.4 Nyingchi, China earthquake.

research mentioned above. The first one has to do with the temporal resolution of the InSAR deformation. The response of hillslope to external stresses is not necessarily instantaneous all the time. For instance, earthquakes generate surface displacements at the moment of ground shaking. However, landscape reactions to variations in hydrological conditions could occur with some degrees of lag time, varying from a few days to a few months (Hilley et al., 2004; Zhao et al., 2012). Therefore, a comparison between, for instance, 12-day InSAR deformation from Sentinel-1 and 12-day accumulated precipitation from satellite products may not match, yielding to poor correlations. The second obstacle is linked to the details of the InSAR deformation with respect to the available environmental characteristics. For instance, if one would aim at estimating hillslope deformation mainly on the basis of precipitation data, then Sentinel-1 images would have a spatial resolution of 5 m $\times$ 20 m, whereas satellite-based global rainfall products would have at least a few km grid spacing (e.g., CHIRPS, McNally, 2018: 0.05°; IMERG, Huffman et al., 2019: 0.1°). Therefore, spatial variation in surface deformation may not be accurately captured by such coarse precipitation estimates.

Our study aims at simultaneously minimising both limitations and proposes an explainable, regional-scale predictive model for InSAR-derived hillslope deformations. This is achieved via the first multivariate model in the literature that targets mean velocities in satellite Line of Sight (V_{LOS}) direction. Our result shows that the contributions of different terrain and environmental characteristics can be estimated and further used for predictive purposes. As a result, this method has the potential to lift the curtains for a number of spatio-temporal models aimed at estimating V_{LOS} in future scenarios.

2. Methods

2.1. Generating the dependent variable of the model

To identify hillslope deformation velocities, we implemented a standard time series InSAR approach i.e. PSI for PS deformation time series estimation (Ferretti et al., 2001). We divided SAR data into four sequential time stacks (TS1–4, see Table S1–4). These correspond to the intra-seismic phases between earthquake of magnitude equal or >5.0 and the next, from 2017 to 2021. Specifically, we used 125 Sentinel-1A satellite SAR images acquired between November 2017 and July 2022, in VV polarization channel. Sentinel-1A satellite is operated in C band (5.6 cm), and has a 12-day repeat cycle and delivers SAR images with 5 $\times$ 20 m spatial resolution. We collected data in descending orbital direction, with path 4 and frame 491, which cover the area affected by the 2017 Nyingchi earthquake region (Fig. 1).

Per time stack, during PSI processing, we selected the most optimal master acquisition (Zebker and Villasenor, 1992) to mitigate spatial and temporal decorrelation. We used the 30 m Shuttle Radar Topography Mission (SRTM) digital elevation model to estimate the topographic phase, and GACOS (Generic Atmospheric Correction Online Service; Yu et al., 2018) to remove the atmospheric phase, and applied 3D phase unwrapping (Hooper et al., 2018) to generate PS deformation time series estimation in LOS. Assuming all PS generally have linear behaviour over time and the InSAR observation errors are within an allowable range, we employed a linear function of time to describe PS deformation time series. Then the mean velocity in LOS, V_{LOS}, can be considered as the unknown parameter in the observation function shown below:

Table 1
Summary of independent variables.

Variable	Abbreviation	Reference	Unit
Slope steepness (mean and standard deviation per SU)	$Slope_{\mu}$ / $Slope_{\sigma}$	Zevenbergen and Thorne, 1987	degree
Distance to quaternary faults (mean)	$dist2fault_{\mu}$	Wang et al., 2017	m
Peak Ground Acceleration	PGA	Worden and Wald, 2016	g_n
Total precipitation	–	Funk et al., 2015	mm
Plan curvature (mean and standard deviation per SU)	$planCurv_{\mu}$ / $planCurv_{\sigma}$	Heerdegen and Beran, 1982	1/m
Profile curvature (mean and standard deviation per SU)	$profCurv_{\mu}$ / $profCurv_{\sigma}$	Heerdegen and Beran, 1982	1/m
Vector ruggedness measure	VRM_{μ} / VRM_{σ}	Sappington et al., 2007	unitless
Fraction of snow cover	SnowCov	FLDAS Noah Land Surface Model; McNally, 2018	%
Maximum temperature difference	$Temp_{diff}$	Wan et al., 2021	°C
Lithology	–	Wang et al., 2017	–

$$d^i_{LOS} = B^i_t V_{LOS}$$

where d^i_{LOS} represents the LOS deformation value of a PS at the ith acquisition, and B^i_t represents the temporal baseline between the master and slave at the ith acquisition. Since d^i_{LOS} and B^i_t are known based on PSI processing, calculating V_{LOS} is straightforward.

2.2. Generating mapping units and independent variables of the model

We used r.slopunits (Alvioli et al., 2016) to generate slope units (SUs), which is the mapping unit we opted for this research. There, we used SRTM digital elevation model, with 1 arc-second spatial resolution (NASA JPL, 2013) to generate SUs. We aggregated all dependent and independent variables per SU.

We used 10 parameters to generate our independent variables (Table 1), these have been mostly selected according to the literature on landslide susceptibility and hazard assessment (Budimir et al., 2015; van Westen et al., 2006). Our assumption is that the geologic, topographic, seismic, meteorological and climatic conditions controlling hillslope stability could also play role in hillslope deformation rates. Therefore, the idea is for these 10 parameters to be able to reflect the combined effect of static and dynamic environmental characteristics that the examined landscape had to undergo from TS1 to TS4. If the spatial resolution of a given parameter is overall finer than SU, we calculate both the mean and standard deviation of cell values falling into each SU. Specifically, this was the procedure we followed for the parameters derived from the digital elevation model.

2.3. Developing the data-driven model

To model the spatial distribution of mean V_{LOS}, we adopted a Generalized Additive Mixed Model structure framed in a Bayesian context. This was achieved by using the Integrated Nested Laplacian Approximation (INLA, Bakka et al., 2018) and its implementation in the inlabru package (Bachl et al., 2019).

The model we opted for can be denoted as follows:

$$V_{LOS} = B_0 + \sum(B_n{*}X_n) + f_1(Slope_{\mu}) + f_2(dist2Fault) + f_3(PGA) + f_4(Total\ precipitation) + f_5(planCurv) + f_6(profCurv)$$

where B_0 is the global intercept, B_n are the regression coefficients estimated for the n explanatory variables used linearly, f_1 to f_6 are the nonlinear models applied to the respective ordinal variables and f_7 is the nonlinear model applied to the categorical information carried by each independent geological class.

Because of the Bayesian nature of our model, each term mentioned above returned a distribution of regression coefficients. These have been used to generate 1000 simulations over the spatiotemporal domain represented by TS2, TS3 and TS4, from which we extracted mean predicted values and the 95% width of their credible interval.

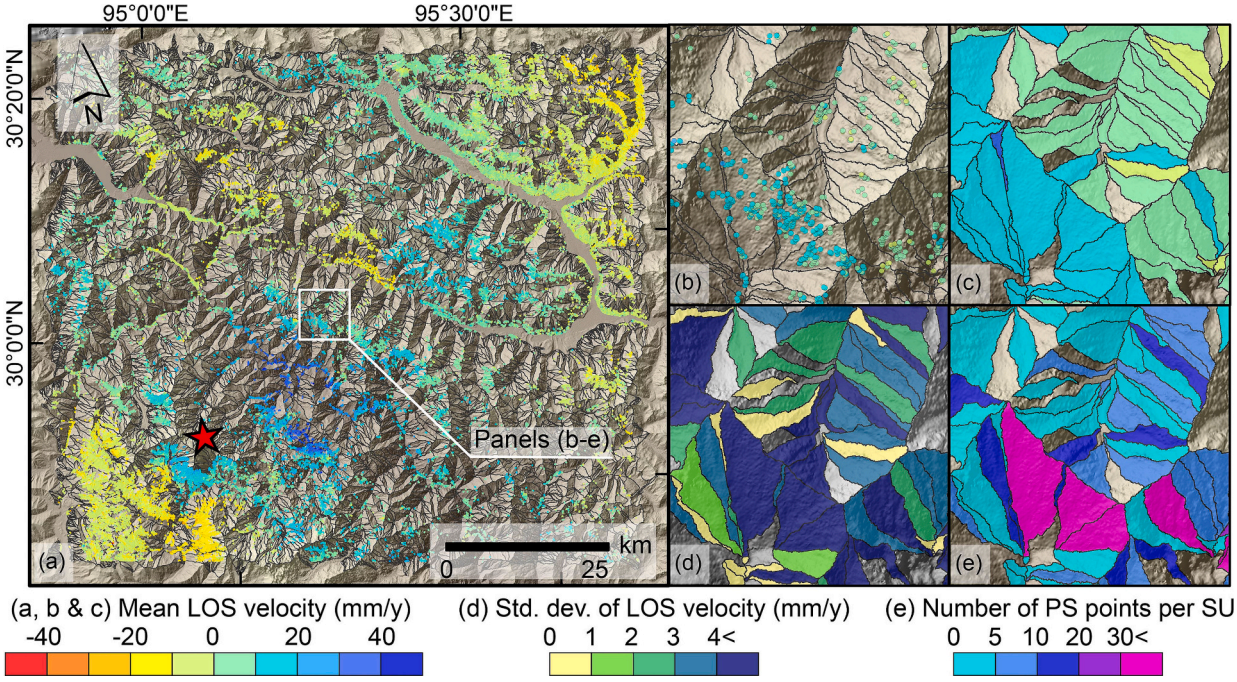

Fig. 2. Panels showing (a-b) spatial distribution of PS points over Sus, (c) aggregated mean LOS velocities, (d) their standard deviations and (e) number of PS points for SU. Red star indicates the epicentre of the 2017 Nyingchi earthquake. (For interpretation of the references to colour in this figure legend, the reader is referred to the web version of this article.)

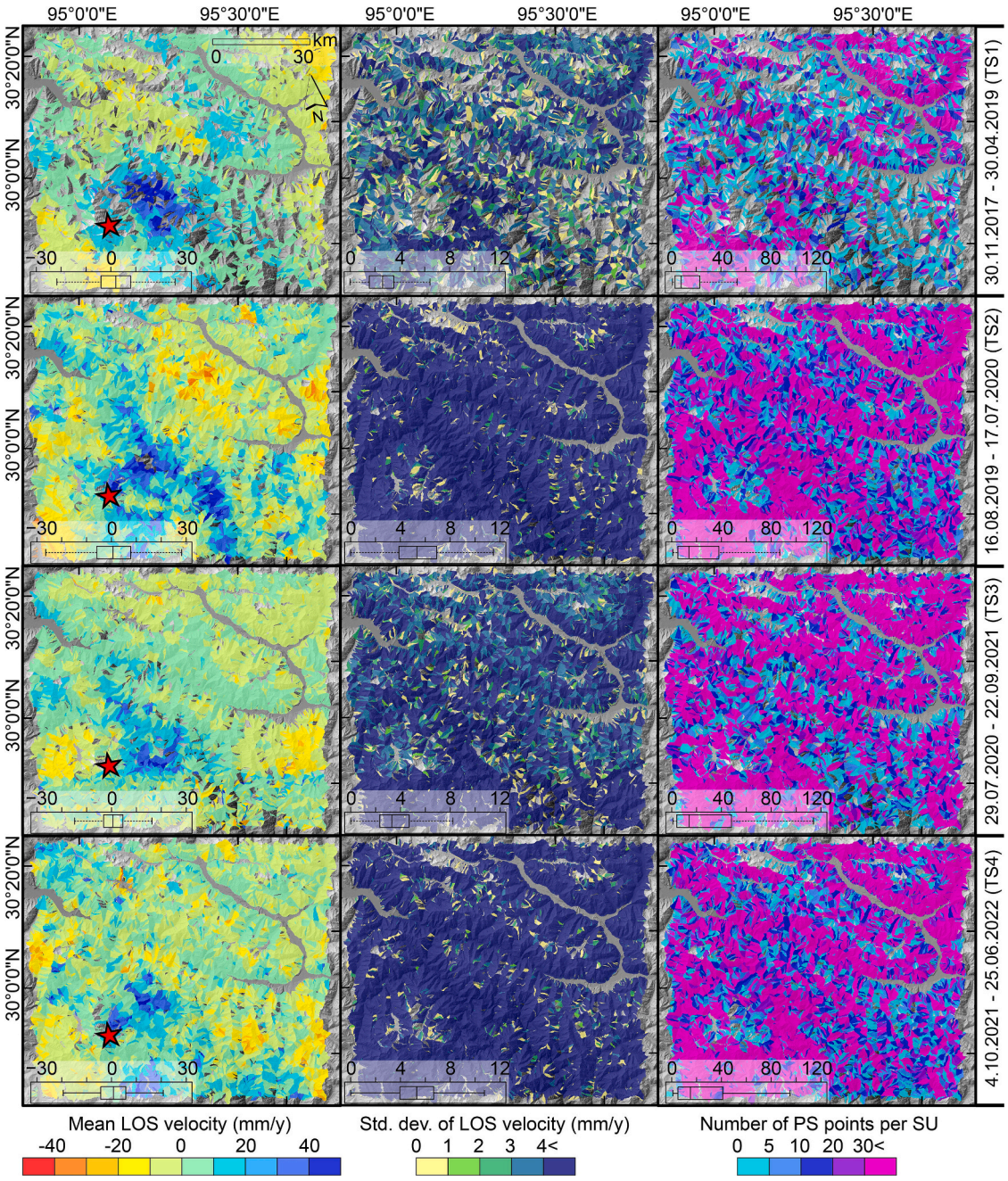

Fig. 3. Columns from left to right showing mean LOS velocities, their standard deviation aggregated for SUs and the number of PS points per SU, respectively. Rows from top to bottom represent four different time series (TS1–4) chronologically in ascending order. Red star indicates the epicentre of the 2017 Nyingchi earthquake. (For interpretation of the references to colour in this figure legend, the reader is referred to the web version of this article.)

As for the cross-validation routines we explored, the 10-fold one worked by randomly sub-setting the TS1 data into ten balanced sample groups. As their random selection was constrained to select a given SU only once, the union of the ten sample groups returns the initial TS2 data. The leave-one-out procedure also iteratively subsets the TS2 spatial domain but it does it by taking one SU out at a time, repeating the same procedure until all SUs have been used for predictive purposes.

3. Results

Through Persistent Scatterer Interferometry (Ferretti et al., 2001), we generated Persistent Scatterer (PS) points and further derived line-of-sight deformation time series. From these, we computed mean V_{LOS} for the area (80 km × 95 km) affected by the 2017 Mw 6.7 Nyingchi (China) earthquake (Fig. 1). Overall, 1800 co-seismic landslides were triggered in response to this earthquake (Zhao et al., 2019), after which, six subsequent ruptures (Mw ≥ 5.0) shook the same area. In such cases, the potential rapid deformation caused by the ground motion could decrease the coherence of interferograms. To ensure that this negative influence (Bekaert et al., 2020) would be minimised, we scanned four different stacks of Sentinel-1 images acquired between earthquakes (Table S1) and generated four deformation Time Stacks (TS1–4).

Such data was then used to develop a data-driven model where the mean V_{LOS} would be regressed against a set of terrain and environmental factors. We stress here the spatial nature of the multivariate model we envisioned, as it is inspired by other standard slope instability models typical of the susceptibility (Steger et al., 2021) and hazard (Aguilera et al., 2022) contexts. Specifically, we used a Bayesian version of a

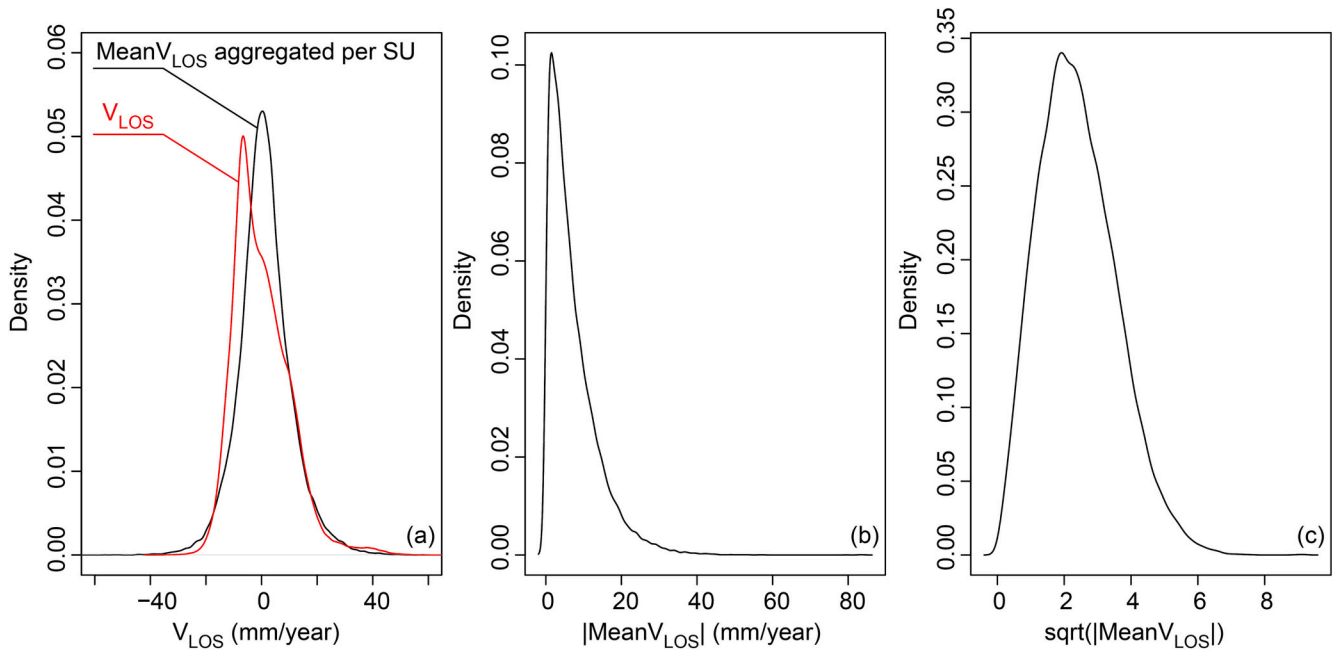

Fig. 4. Frequency density distributions of (a) V_{LOS}, (b) absolute V_{LOS} and (c) the square root of absolute V_{LOS} values generated for Time Series 1 (TS1).

Generalized Additive Mixed Model (GAMM, Beale et al., 2010; Lin and Zhang, 1999; Lombardo et al., 2021; Wood, 2006). The mapping units we chose consisted of slope units (SU, Figs. 2a-b), a geomorphological object bound in between sub-catchment divides and streamlines (Alvioli et al., 2016). Notably, their geographic expression does not include flat areas. At the SU level, we aggregated each predictor under consideration by computing mean and standard deviation values (see Table 1 in the Method section). We then applied the same aggregation to the mean V_{LOS} estimated for any PS points falling within a SU (Figs. 2c-d), also storing the PS count in the process (Fig. 2e).

A geographical overview of the same parameters can be seen in Fig. 3 for each of the time stacks under consideration. There, the largest deformation is shown in the case of TS1, in the proximity of the 2017 Nyingchi earthquake epicentre and it fades away in the following time

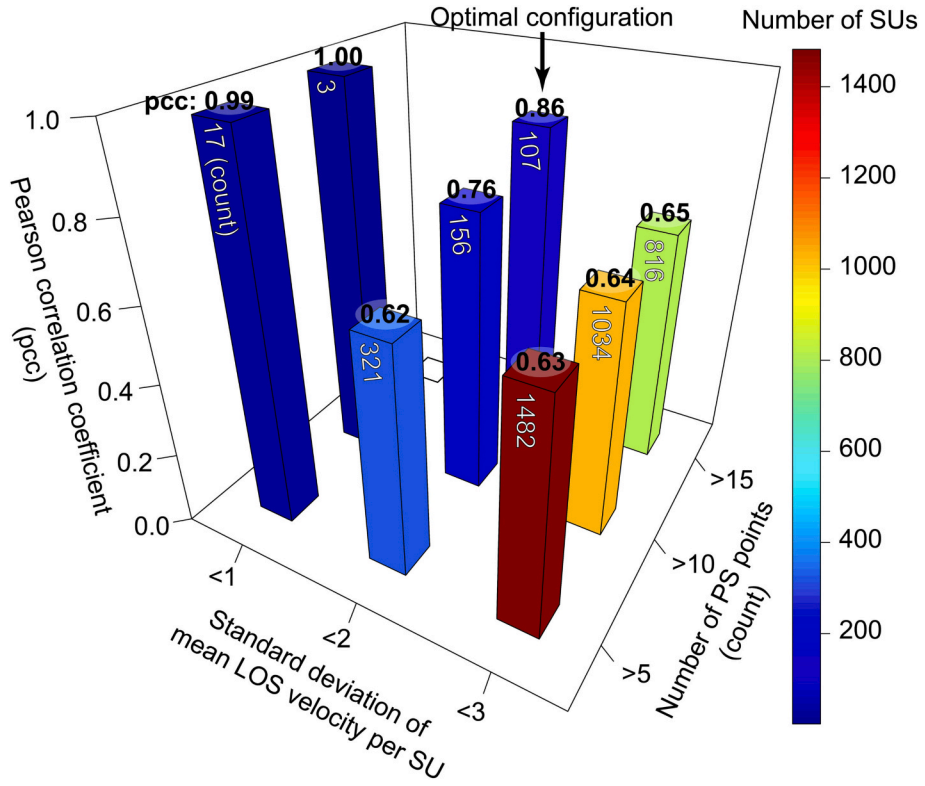

Fig. 5. Pearson correlation coefficients of the fitted model calculated based on different sampling strategies depending on PS count and V_{LOS} standard deviation SU.

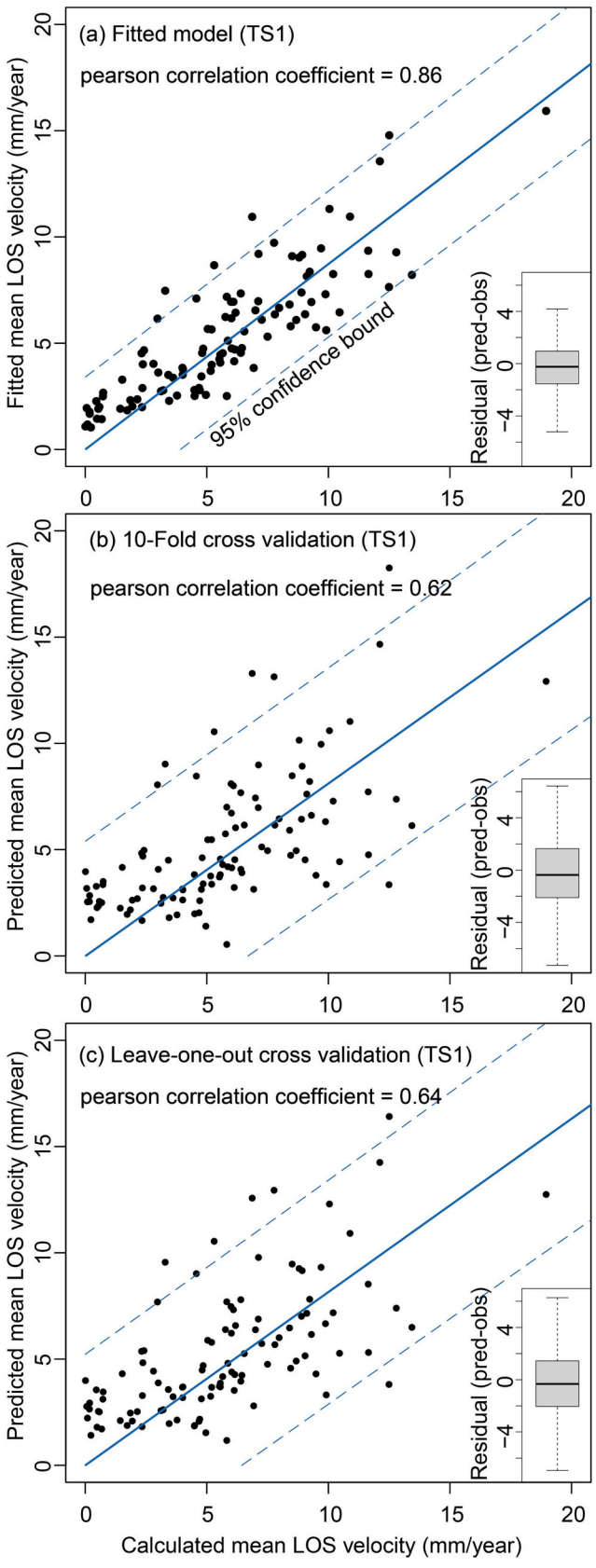

Fig. 6. Goodness of fit calculated for (a) the fitted model, (b) 10-fold cross validation and (c) leave-one-out cross validation.

stacks. As for the intra-earthquake variability of the V_{LOS}, TS1 also shows the least standard deviation values among the four time stacks. Aside from the quality of the response variable information, data related to TS1 were also equipped with ground motion information. Specifically, the U.S. Geological Survey (USGS) ShakeMap service released a peak ground acceleration (PGA) map for the Nyingchi earthquake (Worden and Wald, 2016), although this is not the case for the following earthquakes in this region. For the above reasons, we opted to test our multivariate regression model on TS1 data. Applications to TS2, TS3 and TS4 will be elaborated in the Discussion section.

The raw V_{LOS} appears normally distributed, with values that ranged from −60 to 60 mm/year (Fig. 4a). However, negative and positive V_{LOS} values may carry the same meaning because the sign of V_{LOS} is an indication of the hillslope motion either away from the satellite or toward it (Aslan et al., 2020). For this reason, we initially transformed it by extracting its absolute values, after which the distribution became much more heavy tailed (Fig. 4b). To bring it back to a shape suitable for a Gaussian model to be run, we then further transformed it by taking the square root (Fig. 4c). We then used ten among terrain and environmental factors, featuring six time-invariant and four time-variant properties (Table 1). An initial test over the whole TS1-V_{LOS} data yielded relatively poor goodness-of-fit (pcc = 0.6). As a result, we explored an iterative procedure where we fitted the same model but constrained the SU selection on the basis of two data quality criteria: PS count and standard deviation of the V_{LOS}, respectively calculated for each SU.

The two data quality related parameters were binned into three classes each, returning PS count >5, 10 and 15 per SU, and V_{LOS} standard deviation below 3, 2 and 1 per SU. The resulting nine combinations are shown in Fig. 5, where we also highlighted our optimal configuration. This corresponds to a dataset made of 107 SUs, with a PS count >15 and an admissible V_{LOS} variability measured in <2 mm/year. Its explanatory and predictive capacities are depicted in Fig. 6 where panel (a) indicates an extremely good agreement between observed and fitted V_{LOS}, with a Pearson Correlation Coefficient (pcc) of 0.86. The two following cross-validation schemes shown in panels b (10-Fold) and panel c (leave-one-out), both exceeded a pcc of 0.6.

To interpret the effect of each independent variable, Fig. 7 presents the marginal distributions of each model component, both for the ones modelled linearly and nonlinearly. These have been respectively sorted from the largest contributor to the least one. As a result, one can verify whether the model is producing results that follow assumptions derived from physical considerations. For instance, one can reasonably hypothesise that the largest deformation is to be expected in steeper slopes, where the model actually returns a largely significant and positive regression coefficient (Fig. 7a). The same can be done for the other components. For instance by assuming that the largest slope deformation values should be found close to active faults, something the models confirm with a positive regression coefficient up to few km in Euclidean distance (Fig. 7b). PGA and cumulative rainfall also confirm the same geomorphological reasonability through their respective positive trends (Figs. 7c,d). The two curvatures though mostly align along the zero value, which indicates a negligible contribution to the model (Figs. 7e, f). As for the lithological control over the V_{LOS}, none of the lithological units appears significant (Fig. 7g). However, on average slate and schist contribute to increase the hillslope deformations, as one can expect because of the layered structure of these metamorphic rocks (Marinos and Hoek, 2001). Among the linear variables (Fig. 7h), only the standard deviation of terrain ruggedness (VRM_σ) and fraction of snow cover (SnowCov) appear to be significant (i.e., the distribution does not intersect the zero line). For the former one this indicates that large variations in surface roughness increase surface deformation rates, whereas the later one could be interpreted as a proxy for the seasonally melting snow cover.

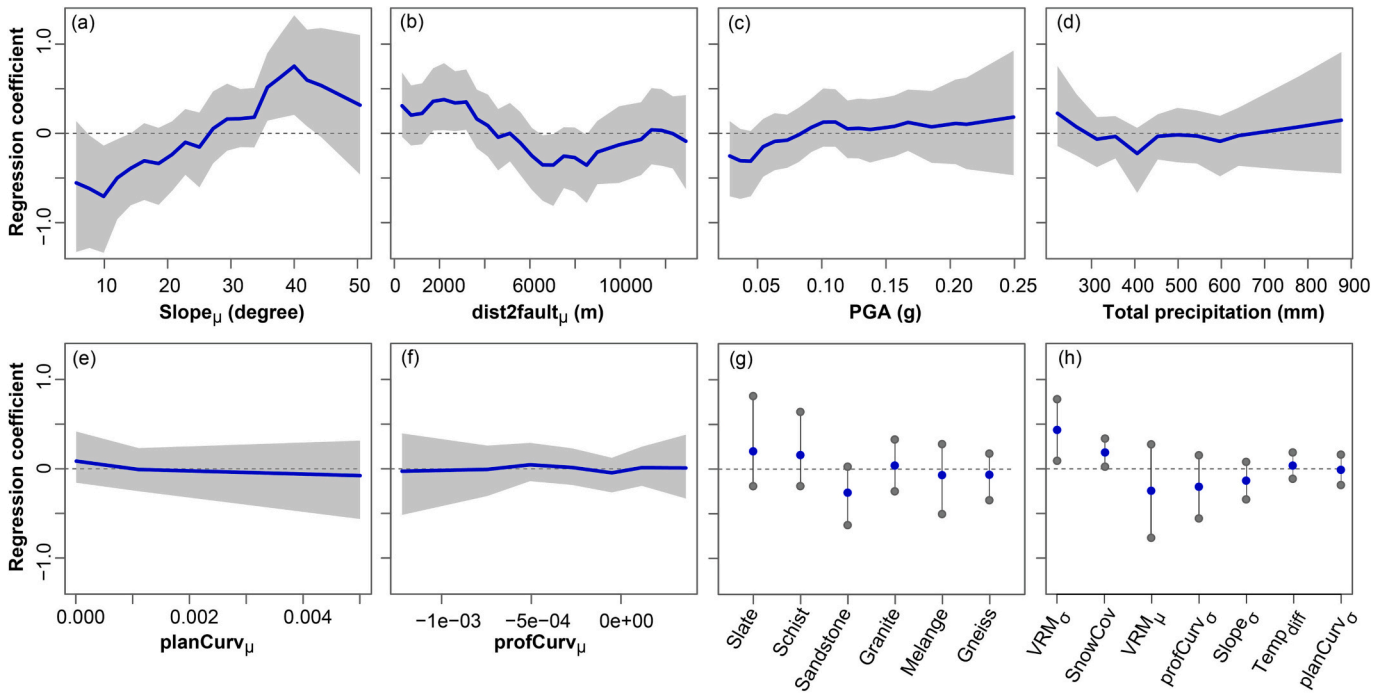

Fig. 7. Summary of non-linear and linear variables regression coefficients. Posterior means are indicated by blue lines and dots in non-linear and linear variables, respectively. Grey-shaded areas and grey dots indicate 95% credible intervals for non-linear and linear variables, respectively. (For interpretation of the references to colour in this figure legend, the reader is referred to the web version of this article.)

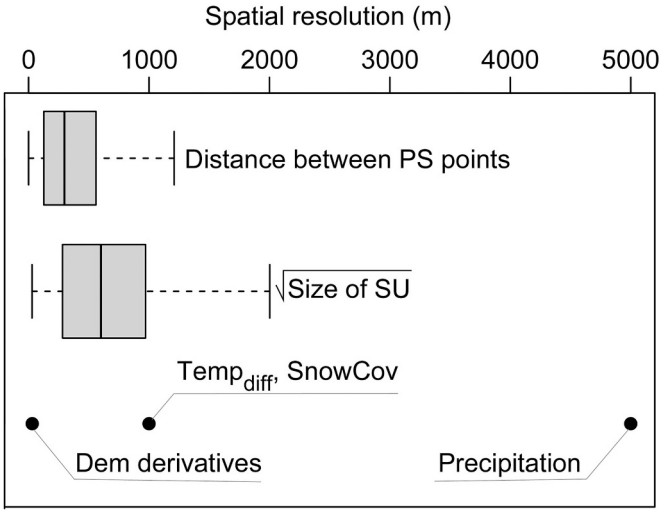

Fig. 8. Spatial characteristics of PS points, SUs and predictive factors used in the analyses. We took the square root of SU areas to bring them to a comparable level with other variables.

4. Discussion and conclusions

This research proposed a predictive model for InSAR-derived surface deformations, capable of addressing two main limitations associated with the temporal and spatial resolutions of the data. Specifically, we used mean V_{LOS} estimated over fixed time windows, these being identified according to earthquake occurrence dates (see Fig. 3). And to obtain suitable explanatory variables, we also extracted climatic conditions representative of the same periods. As for the second limitation, we used SUs as the object to aggregate both dependent and independent variables' information. This procedure aimed at spatially downscaling or upscaling to the same level all the available data (Fig. 8). As a result of this pre-processing step, mixed PS point values were combined at the SU level, raising the question on how reliably this can be done. In fact, large variations in V_{LOS} may exist among PS points falling within the same SU. Another issue to be considered has to do with the number of PS points in a given SU. At times, only a few PS points characterised the mapping unit of our choice. In those cases, even if V_{LOS} values may be similar, they may not be sufficient to represent the movement SU is exhibiting as a whole. In other words, just a couple of PS points may be representative of very local features, thus being difficult to be explained according to a set of coarser explanatory variables. This was the rationale we followed to seek the optimal configuration of PS count and V_{LOS} standard deviation per SU.

Our experiment showed that the spatial distribution of V_{LOS} can be multivariately estimated for SU where the quality of the InSAR signal is rich (number of PS points) and consistent (small variations). Given this constraint, our results also showed that the contribution of each variable to the V_{LOS} could be explored. What is yet to be confirmed is how good such a model could be when extending the prediction both in space and time (i.e., without any constraints to the SU selection). To explore this aspects, we used the fitted model to simulate over the whole study area as well as TS2, TS3 and TS4.

We should stress that the time-variant explanatory variables (total precipitation, average temperature difference and fraction of snow cover) were updated for each of these target time stacks. Regrettably, this could not be done for the PGA maps following the 2017 Nyingchi earthquake because the ShakeMap service only provides PGA estimates for earthquakes of magnitude >5.5. Therefore, we tried to exploit the footprint of ground shaking caused by the 2017 Nyingchi earthquake even in its post-seismic periods. In fact, for strong earthquakes as the one under consideration, the ground shaking could leave a spatial signature on future hillslope deformation patterns up to a few years after the event, a concept commonly referred to as earthquake legacy (Tanyaş et al., 2021). In theory, we could have extended our predictor set to feature a better proxy than the PGA to capture the earthquake legacy. However, there is no current practical solution to this issue, which is the

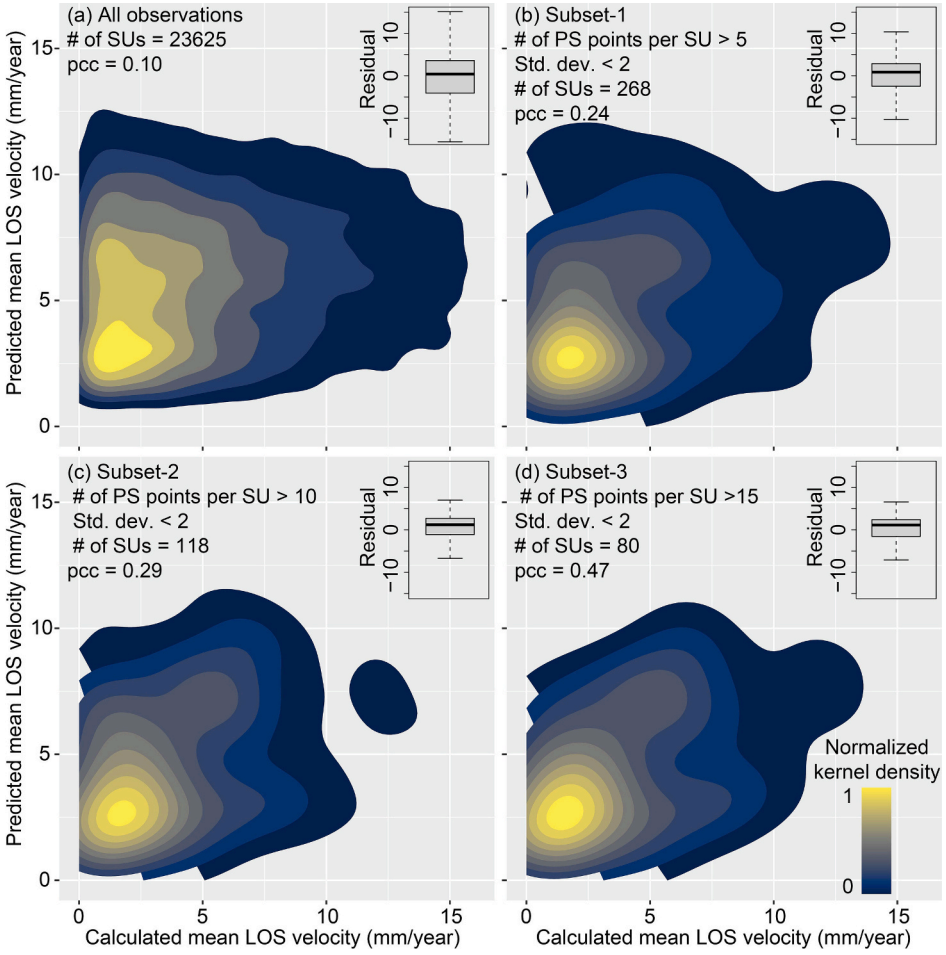

Fig. 9. Summary of space-time predictive model's tests over (a) all SUs in TS2, TS3 and TS4 and (b) SUs where standard deviation<2 and PS counts>5, (c) SUs where standard deviation<2 and PS counts>10 and (d) SUs where standard deviation<2 and PS counts>15.

reason why we opted for the PGA signal both to convey the impulsive stress released during the rupture, as well as the long-term legacy it left on the landscape.

Results show that the predictive capacity of the model is low (pcc = 0.10), although the residuals are still bounded between ±15 mm/year when it is tested over all SUs from TS2, TS3 and TS4 (Fig. 9a). But, if we introduce some constraints based on PS count and standard deviation of the V_{LOS} for the whole space-time domain a gradual improvement becomes increasingly evident. Keeping the same criteria as the ones used to model TS1, we generate Subset-1 (Fig. 9b), Subset-2 (Fig. 9c) and Subset-3 (Fig. 9d), respectively. The modelling performance then increased returning pcc of 0.24, 0.29 and 0.47, respectively. It is also worth mentioning that from Subset-1 to Subset-3 the number of observations decreases while residuals decrease (Fig. 9), which is still the main issue to be addressed before considering this model for operational uses.

Nevertheless, this model has the potential to lay the foundations for a new chapter in the InSAR literature for slope deformation. High quality data was unfortunately not available in our case study, but coupling higher resolution seismic and climatic variables with even finer SUs could significantly improve the overall performance. For instance, 3D numerical earthquake simulations could be used to increase the spatial resolution of ground shaking parameters (Dunham et al., 2022). Similarly, better precipitation data (e.g., CHELSA, Karger et al., 2021: 0.01°) could be integrated in the modelling protocol. The same could apply to the topographic data, by acquiring LIDAR-based high resolution digital elevation models and to generate detailed slope units from.

Author contribution

HT and LL conceptualised the research idea. InSAR analyses were carried out by KH, LC and HT and the data-driven model was developed by LL and HT. HT and LL wrote the first version of the manuscript. LC and KH involved in writing of the final version of manuscript, whereas XH and CL provided feedback on it.

Declaration of Competing Interest

The authors declare no competing interest.

Data availability

Data matrix containing all independent and dependent variables we used in the analyses are available in the supplementary information.

Acknowledgments

The Geospatial Computing Platform of the Center of Expertise in Big Geodata Science (CRIB) (https://crib.utwente.nl) is used for the processing of Sentinel-1 data. We thank Dr. Serkan Girgin for his support in providing the necessary computing infrastructure. The authors gratefully acknowledge support from the National Key R&D Program of China (2022YFC3005704), the National Natural Science Foundation of China (42277143), and the China Scholarship Council (NO. 202107000060).

Appendix A. Supplementary data

Supplementary data to this article can be found online at https://doi.org/10.1016/j.rse.2023.113518.

References

Aguilera, Q., Lombardo, L., Tanyas, H., Lipani, A., 2022. On the prediction of landslide occurrences and sizes via hierarchical neural networks. Stoch. Environ. Res. Risk Assess. https://doi.org/10.1007/s00477-022-02215-0.

Alvioli, M., Marchesini, I., Reichenbach, P., Rossi, M., Ardizzone, F., Fiorucci, F., Guzzetti, F., 2016. Automatic delineation of geomorphological slope units with r. Slopeunits v1.0 and their optimization for landslide susceptibility modeling. Geosci. Model Dev. 9, 3975–3991. https://doi.org/10.5194/gmd-9-3975-2016.

Aslan, G., Foumelis, M., Raucoules, D., De Michele, M., Bernardie, S., Cakir, Z., 2020. Landslide mapping and monitoring using persistent scatterer interferometry (PSI) technique in the french Alps. Remote Sens. https://doi.org/10.3390/rs12081305.

Bachl, F.E., Lindgren, F., Borchers, D.L., Illian, J.B., 2019. Inlabru: an R package for bayesian spatial modelling from ecological survey data. Methods Ecol. Evol. 10, 760–766. https://doi.org/10.1111/2041-210X.13168.

Bakka, H., Rue, H., Fuglstad, G.-A., Riebler, A., Bolin, D., Illian, J., Krainski, E., Simpson, D., Lindgren, F., 2018. Spatial modeling with R-INLA: a review. WIREs Comput. Stat. 10, e1443 https://doi.org/10.1002/wics.1443.

Barra, A., Monserrat, O., Mazzanti, P., Esposito, C., Crosetto, M., Scarascia Mugnozza, G., 2016. First insights on the potential of Sentinel-1 for landslides detection. Geomatics. Nat. Hazards Risk 7, 1874–1883. https://doi.org/10.1080/19475705.2016.1171258.

Beale, C.M., Lennon, J.J., Yearsley, J.M., Brewer, M.J., Elston, D.A., 2010. Regression analysis of spatial data. Ecol. Lett. 13, 246–264. https://doi.org/10.1111/j.1461-0248.2009.01422.x.

Bekaert, D.P.S., Handwerger, A.L., Agram, P., Kirschbaum, D.B., 2020. InSAR-based detection method for mapping and monitoring slow-moving landslides in remote regions with steep and mountainous terrain: an application to Nepal. Remote Sens. Environ. 249, 111983 https://doi.org/10.1016/j.rse.2020.111983.

Bontemps, N., Lacroix, P., Larose, E., Jara, J., Taipe, E., 2020. Rain and small earthquakes maintain a slow-moving landslide in a persistent critical state. Nat. Commun. 11, 1–10. https://doi.org/10.1038/s41467-020-14445-3.

Budimir, M.E.A., Atkinson, P.M., Lewis, H.G., 2015. A systematic review of landslide probability mapping using logistic regression. Landslides 12, 419–436. https://doi.org/10.1007/s10346-014-0550-5.

Chaussard, E., Amelung, F., Abidin, H., Hong, S.-H., 2013. Sinking cities in Indonesia: ALOS PALSAR detects rapid subsidence due to groundwater and gas extraction. Remote Sens. Environ. 128, 150–161. https://doi.org/10.1016/j.rse.2012.10.015.

Chen, Yi, He, Y., Zhang, L., Chen, Youdong, Pu, H., Chen, B., Gao, L., 2021. Prediction of InSAR deformation time-series using a long short-term memory neural network. Int. J. Remote Sens. 42, 6919–6942. https://doi.org/10.1080/01431161.2021.1947540.

Cigna, F., Tapete, D., 2021. Present-day land subsidence rates, surface faulting hazard and risk in Mexico City with 2014–2020 Sentinel-1 IW InSAR. Remote Sens. Environ. 253, 112161 https://doi.org/10.1016/j.rse.2020.112161.

Costantini, M., Minati, F., Trillo, F., Ferretti, A., Novali, F., Passera, E., Dehls, J., Larsen, Y., Marinkovic, P., Eineder, M., Brcic, R., Siegmund, R., Kotzerke, P., Probeck, M., Kenyeres, A., Proietti, S., Solari, L., Andersen, H.S., 2021. European Ground Motion Service (EGMS). In: 2021 IEEE International Geoscience and Remote Sensing Symposium IGARSS, pp. 3293–3296. https://doi.org/10.1109/IGARSS47720.2021.9553562.

Crosetto, M., Solari, L., Balasis-Levinsen, J., Bateson, L., Casagli, N., Frei, M., Oyen, A., Moldestad, D.A., Mróz, M., 2021. Deformation monitoring at european scale: the copernicus ground motion service. Int. Arch. Photogramm. Remote. Sens. Spat. Inf. Sci. XLIII-B3-2, 141–146. https://doi.org/10.5194/isprs-archives-XLIII-B3-2021-141-2021.

Dille, A., Kervyn, F., Handwerger, A.L., d'Oreye, N., Derauw, D., Mugaruka Bibentyo, T., Samsonov, S., Malet, J.-P., Kervyn, M., Dewitte, O., 2021. When image correlation is needed: unravelling the complex dynamics of a slow-moving landslide in the tropics with dense radar and optical time series. Remote Sens. Environ. 258, 112402 https://doi.org/10.1016/j.rse.2021.112402.

Ding, Q., Shao, Z., Huang, X., Altan, O., Zhuang, Q., Hu, B., 2021. Monitoring, analyzing and predicting urban surface subsidence: a case study of Wuhan City, China. Int. J. Appl. Earth Obs. Geoinf. 102, 102422 https://doi.org/10.1016/j.jag.2021.102422.

Dunham, A.M., Kiser, E., Kargel, J.S., Haritashya, U.K., Watson, C.S., Shugar, D.H., Hughes, A., DeCelles, P.G., 2022. Topographic control on ground motions and landslides from the 2015 Gorkha earthquake. Geophys. Res. Lett. 49, e2022GL098582 https://doi.org/10.1029/2022GL098582.

Ferretti, A., Prati, C., Rocca, F., 2001. Permanent scatterers in SAR interferometry. IEEE Trans. Geosci. Remote Sens. 39, 8–20. https://doi.org/10.1109/36.898661.

Funk, C., Peterson, P., Landsfeld, M., Pedreros, D., Verdin, J., Shukla, S., Husak, G., Rowland, J., Harrison, L., Hoell, A., Michaelsen, J., 2015. The climate hazards infrared precipitation with stations—a new environmental record for monitoring extremes. Sci. Data 2, 150066. https://doi.org/10.1038/sdata.2015.66.

Gaddes, M.E., Hooper, A., Bagnardi, M., Inman, H., Albino, F., 2018. Blind signal separation methods for InSAR: the potential to automatically detect and monitor signals of volcanic deformation. J. Geophys. Res. Solid Earth 123, 10,210–226,251. https://doi.org/10.1029/2018JB016210.

Haghshenas Haghighi, M., Motagh, M., 2019. Ground surface response to continuous compaction of aquifer system in Tehran, Iran: results from a long-term multi-sensor InSAR analysis. Remote Sens. Environ. 221, 534–550. https://doi.org/10.1016/j.rse.2018.11.003.

He, Y., Yan, H., Yang, W., Yao, S., Zhang, L., Chen, Y., Liu, T., 2022. Time-series analysis and prediction of surface deformation in the Jinchuan Mining Area, Gansu Province, by Using InSAR and CNN–PhLSTM Network. IEEE J. Sel. Top. Appl. Earth Obs. Remote Sens. 15, 6732–6751. https://doi.org/10.1109/JSTARS.2022.3198728.

Heerdegen, R.G., Beran, M.A., 1982. Quantifying source areas through land surface curvature and shape. J. Hydrol. 57, 359–373. https://doi.org/10.1016/0022-1694(82)90155-X.

Hilley, E.G., Roland, B., Alessandro, F., Fabrizio, N., Fabio, R., 2004. Dynamics of slow-moving landslides from permanent scatterer analysis. Science 304, 1952–1955. https://doi.org/10.1126/science.1098821.

Hooper, A., Bekaert, D., Ekbal, H., Spaans, K., 2018. StaMPS/MTI manual: Version 4.1 b. Sch. Earth Environ. Univ, Leeds. Retrieved Oct. 15, 2019.

Huffman, G., Stocker, E.F., Nelkin, E.J., Tan, J., 2019. In: Savtchenko, Andrey (Ed.), GPM IMERG Final Precipitation L3 1 day 0.1 degree x 0.1 degree V06 [WWW Document]. Goddard Earth Sci. Data Inf. Serv. Cent. (GES DISC), Greenbelt, MD. https://doi.org/10.5067/GPM/IMERGDF/DAY/06.

Intrieri, E., Raspini, F., Fumagalli, A., Lu, P., Del Conte, S., Farina, P., Allievi, J., Ferretti, A., Casagli, N., 2018. The maoxian landslide as seen from space: detecting precursors of failure with Sentinel-1 data. Landslides 15, 123–133. https://doi.org/10.1007/s10346-017-0915-7.

Karger, D.N., Wilson, A.M., Mahony, C., Zimmermann, N.E., Jetz, W., 2021. Global daily 1 km land surface precipitation based on cloud cover-informed downscaling. Sci. Data 8, 307. https://doi.org/10.1038/s41597-021-01084-6.

Lacroix, P., Handwerger, A.L., Bièvre, G., 2020. Life and death of slow-moving landslides. Nat. Rev. Earth Environ. 1, 404–419. https://doi.org/10.1038/s43017-020-0072-8.

Lin, X., Zhang, D., 1999. Inference in generalized additive mixed models by using smoothing splines. J. R. Stat. Soc. Ser. B Statist. Methodol. 61, 381–400.

Lombardo, L., Mai, P.M., 2018. Presenting logistic regression-based landslide susceptibility results. Eng. Geol. 244, 14–24. https://doi.org/10.1016/j.enggeo.2018.07.019.

Lombardo, L., Tanyas, H., Huser, R., Guzzetti, F., Castro-Camilo, D., 2021. Landslide size matters: a new data-driven, spatial prototype. Eng. Geol. 293, 106288 https://doi.org/10.1016/j.enggeo.2021.106288.

Ma, P., Zhang, F., Lin, H., 2020. Prediction of InSAR time-series deformation using deep convolutional neural networks. Remote Sens. Lett. 11, 137–145. https://doi.org/10.1080/2150704X.2019.1692390.

Marinos, P., Hoek, E., 2001. Estimating the geotechnical properties of heterogeneous rock masses such as flysch. Bull. Eng. Geol. Environ. 60, 85–92. https://doi.org/10.1007/s100640000090.

Massonnet, D., Feigl, K.L., 1998. Radar interferometry and its application to changes in the Earth's surface. Rev. Geophys. 36, 441–500. https://doi.org/10.1029/97RG03139.

McNally, A., 2018. FLDAS Noah Land Surface Model L4 Global Monthly 0.1 x 0.1 degree (MERRA-2 and CHIRPS). Goddard Earth Sciences Data and Information Services Center (GES DISC), Greenbelt, MD, USA. https://doi.org/10.5067/5NHC22T9375G.

NASA JPL, 2013. NASA Shuttle Radar Topography Mission United States 1 Arc Second. NASA EOSDIS Land Processes DAAC, USGS Earth Resources Observation and Science (EROS) Center, Sioux Falls, South Dakota. Accessed date: 1 December 2019. [WWW Document]. https://lpdaac.usgs.gov.

Palmer, J., 2017. Creeping earth could hold secret to deadly landslides. Nature 548. https://doi.org/10.1038/548384a.

Sappington, J.M., Longshore, K.M., Thompson, D.B., 2007. Quantifying landscape ruggedness for animal habitat analysis: a case study using Bighorn sheep in the Mojave Desert. J. Wildl. Manag. 71, 1419–1426. https://doi.org/10.2193/2005-723.

Steger, S., Mair, V., Kofler, C., Pittore, M., Zebisch, M., Schneiderbauer, S., 2021. Correlation does not imply geomorphic causation in data-driven landslide susceptibility modelling – benefits of exploring landslide data collection effects. Sci. Total Environ. 776, 145935 https://doi.org/10.1016/j.scitotenv.2021.145935.

Tanyaş, H., Kirschbaum, D., Görüm, T., van Westen, C.J., Tang, C., Lombardo, L., 2021. A closer look at factors governing landslide recovery time in post-seismic periods. Geomorphology 391, 107912. https://doi.org/10.1016/j.geomorph.2021.107912.

Tralli, D.M., Blom, R.G., Zlotnicki, V., Donnellan, A., Evans, D.L., 2005. Satellite remote sensing of earthquake, volcano, flood, landslide and coastal inundation hazards. ISPRS J. Photogramm. Remote Sens. 59, 185–198. https://doi.org/10.1016/j.isprsjprs.2005.02.002.

van Westen, C.J., van Asch, T.W.J., Soeters, R., 2006. Landslide hazard and risk zonation—why is it still so difficult? Bull. Eng. Geol. Environ. 65, 167–184. https://doi.org/10.1007/s10064-005-0023-0.

Wan, Z., Hook, S., Hulley, G., 2021. MODIS/Terra Land Surface Temperature/Emissivity Daily L3 Global 1km SIN Grid V061 [Data set]. NASA EOSDIS Land Processes DAAC. Accessed 2022-10-10 from.

Wang, J., Jiang, L., Niu, B., Ren, J., He, Z., Jin, X., Xie, L., Zhao, L., Liu, R., 2017. In: GDDP, System (Ed.), Spatial database of 1:5 million international geological map of Asia.

Wood, S.N., 2006. Low-rank scale-invariant tensor product smooths for generalized additive mixed models. Biometrics 62, 1025–1036.

Worden, C.B., Wald, D.J., 2016. ShakeMap manual online: Technical manual, user's guide, and software guide. US Geol. Surv. https://doi.org/10.5066/F7D21VPQ.

Xu, W., Jónsson, S., Ruch, J., Aoki, Y., 2016. The 2015 wolf volcano (Galápagos) eruption studied using Sentinel-1 and ALOS-2 data. Geophys. Res. Lett. 43, 9573–9580. https://doi.org/10.1002/2016GL069820.

Yu, C., Li, Z., Penna, N., Crippa, P., 2018. Generic atmospheric correction online service for InSAR (GACOS). In: EGU General Assembly Conference Abstracts, p. 11007.

Zebker, H.A., Villasenor, J., 1992. Decorrelation in interferometric radar echoes. IEEE Trans. Geosci. Remote Sens. 30, 950–959. https://doi.org/10.1109/36.175330.
Zevenbergen, L.W., Thorne, C.R., 1987. Quantitative analysis of land surface topography. Earth Surf. Process. Landforms 12, 47–56. https://doi.org/10.1002/esp.3290120107.
Zhao, B., Li, W., Wang, Y., Lu, J., Li, X., 2019. Landslides triggered by the ms 6.9 nyingchi earthquake, China (18 november 2017): analysis of the spatial distribution and occurrence factors. Landslides 16, 765–776. https://doi.org/10.1007/s10346-019-01146-2.
Zhao, C., Lu, Z., Zhang, Q., de la Fuente, J., 2012. Large-area landslide detection and monitoring with ALOS/PALSAR imagery data over northern California and southern Oregon, USA. Remote Sens. Environ. 124, 348–359. https://doi.org/10.1016/j.rse.2012.05.025.